



Science Arts & Métiers (SAM)

is an open access repository that collects the work of Arts et Métiers Institute of Technology researchers and makes it freely available over the web where possible.

This is an author-deposited version published in: <https://sam.ensam.eu>
Handle ID: [.http://hdl.handle.net/10985/22743](http://hdl.handle.net/10985/22743)

To cite this version :

Alessio TREBBI, Ekaterina MUKHINA, Nathanaël CONNESSON, Mathieu BAILET, Antoine PERRIER, Yohan PAYAN, Pierre-Yves ROHAN - MR-based quantitative measurement of human soft tissue internal strains for pressure ulcer prevention - Medical Engineering and Physics - Vol. 108, p.103888 - 2022

Any correspondence concerning this service should be sent to the repository

Administrator : scienceouverte@ensam.eu



1 **MR-based quantitative measurement of human soft tissue internal strains for**
2 **pressure ulcer prevention**

3

4 **Authors:**

5 **Alessio Trebbi***

6 Univ. Grenoble Alpes, CNRS, TIMC, 38000 Grenoble, France.

7 Alessio.Trebbi@univ-grenoble-alpes.fr

8 **Ekaterina Mukhina**

9 Univ. Grenoble Alpes, CNRS, TIMC, 38000 Grenoble, France.

10 ekaterina.mukhina@univ-grenoble-alpes.fr

11 **Pierre-Yves Rohan**

12 Institut de Biomécanique Humaine Georges Charpak, Arts et Métiers ParisTech, 151 bd de l'Hôpital,
13 75013. Paris, France

14 Pierre-Yves.ROHAN@ensam.eu

15 **Nathanaël Connesson**

16 Univ. Grenoble Alpes, CNRS, TIMC, 38000 Grenoble, France.

17 nathanael.connesson@univ-grenoble-alpes.fr

18 **Mathieu Bailet**

19 TwInsight, 38000 Grenoble, France

20 mathieu.bailet@twinsight-medical.com

21 **Antoine Perrier**

22 Univ. Grenoble Alpes, CNRS, TIMC, 38000 Grenoble, France

23 Groupe hospitalier Diaconesses–Croix Saint-Simon, 75020 Paris, France

24 TwInsight, 38000 Grenoble, France

25 perrier.antoine@gmail.com

26 **Yohan Payan**

27 Univ. Grenoble Alpes, CNRS, TIMC, 38000 Grenoble, France

28 Yohan.Payan@univ-grenoble-alpes.fr

29

30 *Corresponding author

31

32 **Keywords**

33 DVC, FEM, Heel, Sacrum

34

35 **Abstract**

36 Pressure ulcers are a severe disease affecting patients that are bedridden or in a wheelchair bound for
37 long periods of time. These wounds can develop in the deep layers of the skin of specific parts of the
38 body, mostly on heels or sacrum, making them hard to detect in their early stages.

39 Strain levels have been identified as a direct danger indicator for triggering pressure ulcers. Prevention
40 could be possible with the implementation of subject-specific Finite Element (FE) models. However,
41 generation and validation of such FE models is a complex task, and the current implemented
42 techniques offer only a partial solution of the entire problem considering only external displacements
43 and pressures, or cadaveric samples.

44 In this paper, we propose an *in vivo* solution based on the 3D non-rigid registration between two
45 Magnetic Resonance (MR) images, one in an unloaded configuration and the other deformed by means
46 of a plate or an indenter. From the results of the image registration, the displacement field and
47 subsequent strain maps for the soft tissues were computed. An extensive study, considering different
48 cases (on heel pad and sacrum regions) was performed to evaluate the reproducibility and accuracy of
49 the results obtained with this methodology.

50 The implemented technique can give insight for several applications. It adds a useful tool for better
51 understanding the propagation of deformations in the heel soft tissues that could generate pressure
52 ulcers. This methodology can be used to obtain data on the material properties of the soft tissues to
53 define constitutive laws for FE simulations and finally it offers a promising technique for validating FE
54 models.

55

56 **1. Introduction**

57 Pressure ulcers are serious injuries generated by prolonged mechanical loadings applied on soft
58 tissues. Most of the pressure ulcers occur on the heel and on the sacrum as these locations are loaded
59 when patients are bedridden or wheelchair bound for long periods of time [1][2][3]. Ulceration
60 requires high amounts of resources from the nursing cares and time to be healed and therefore
61 represents a serious problem to the individual and the health care system[4]. In the worst cases, these
62 complications lead to amputations and death. Depending on the type of external mechanical load,
63 anatomy and tissue integrity, pressure ulcers can start superficially or deep within the soft tissues.
64 Superficial wounds are formed on the skin surface and progress downwards, making them easy to
65 identify in the early stages with solutions that can be promptly adopted to stop their progression. On
66 the other hand, deep tissue injuries arise in muscle or fat layers around bony prominences and are
67 often caused by high strains of the biological tissues. A value of 0.65 for the Green Lagrange (GL)
68 maximal shear strain was provided by Ceelen et al. as a threshold that should not be exceeded to avoid
69 any pressure ulcer [5]. This last case represents a major threat due to the impossibility to quickly
70 identify the ulcer formation and promptly take action [6]. For this purpose, techniques to monitor the
71 level of strain in the deep layers of the skin and underlying soft tissues are currently extensively
72 investigated in the literature [7].

73 A common methodology to estimate internal tissue strains relies on FE modeling, with simulations that
74 reproduce the body part morphology, tissue biomechanical parameters and the type of loading
75 [8][9][10]. However, validation of FE simulations of the mechanical response of *in vivo* biological tissues
76 to external mechanical loads has always been problematic. Keenan et al. report that none of the
77 current heel models have been properly validated against independent experimental measurements
78 and that further work is needed to develop models that are well validated to draw reliable clinical
79 conclusions [8]. Regarding the buttock region, Savonnet et al. reached a similar conclusion stating that
80 only few models were validated with experimental observations [9]. Because direct validation of
81 internal mechanical strains is a challenging problem, many research works proposed to evaluate FE
82 models of the foot in terms of their capacity to predict interface plantar pressure by comparing the

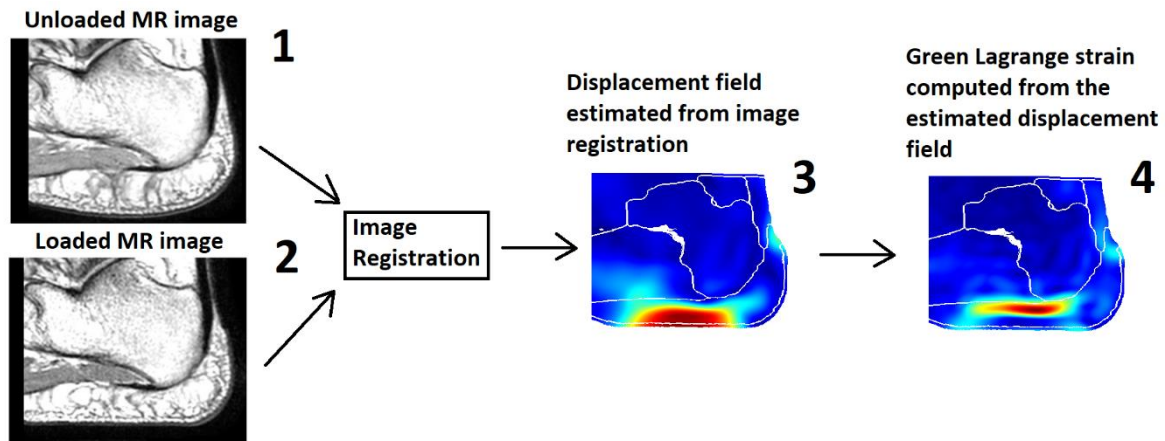
83 contact pressure predicted by the FE model with the measurements from pressure mattresses [11].
84 Yet, as observed in Macron et al. [12] on data from 13 healthy volunteers, interface pressure
85 distributions do not correlate with internal strains and one cannot be used to predict the other. This
86 issue was partially addressed by Linder-Granz et al. [13] for a buttock FE model in a study where the
87 authors compared contours of the computational domain in the deformed configuration predicted by
88 the simulations to the ground truth segmented contours obtained from MR images. This comparison,
89 however, considers only the external shape and not the quantity of interest, which is the local internal
90 tissue displacement and associated tissue strains.

91 In an original contribution, Stekelenburg et al. [14] proposed to use MR tagging and phase contrast
92 sequences on a rat leg model under indentation to assess local tissue displacements and compute the
93 associated tissue strains. The main restriction of this approach is that the indenter (used inside the MR
94 machine to deform the tissue) has to be applied rapidly and repetitively as the tagging grid fades within
95 1 s because of MR relaxation. This requirement can be complex to overcome with an MR compatible
96 device. Moreover, this constraint does not allow for conventional control systems for the application
97 of loads such as gravity, hydrostatic pressure or compression springs [15][16][17]. Additionally, with
98 dynamic loads applied, the viscoelastic properties of the biological tissues could have an impact on the
99 mechanical response, thus increasing the complexity to estimate the tissues passive mechanical
100 properties from the experimental measurements.

101 Digital Volume Correlation (DVC) is an emerging non-invasive technique that allows to characterize
102 experimentally material mechanical response to external loadings by tracking the displacement of
103 natural patterns. From the displacement field, local strains can be computed. Combined with 3D MR
104 images, DVC can, for example, be used to estimate human tissue internal strains [18]. From two MR
105 datasets, one collected in an arbitrary undeformed configuration and another in a deformed
106 configuration, the non-linear transformations that will align the MR volume at rest to the deformed
107 one can be computed using a procedure call Image Registration. To illustrate the process, a graphical
108 summary of the procedure is proposed based on data collected by the authors on the foot (Figure 1).
109 DVC has previously been used in for *in vivo* strain estimation in human intervertebral discs, brain and
110 leg muscles under external mechanical loading [19][20][21].

111 Our group has recently developed an MR-compatible device for applying controlled shearing and
112 normal loads to the human heel pad [16]. With such a device, 3D MR volumes of the heel pad soft
113 tissue can be imaged under various loads applied on the foot sole. This paper aims at describing the
114 methodology proposed by our group to implement DVC on human soft tissues and at estimating the
115 internal strains from the DVC-derived 3D displacement field. The long-term objective is to validate a
116 FE model, in terms of its capacity to predict the localization and the intensity of the strain field in the
117 soft tissues.

118



119
 120 Figure 1 : Scheme of quantitative measurement of soft tissue internal strains obtained from image
 121 registration. Image 1: unloaded configuration. Image 2: Loaded configuration. The image registration
 122 estimates the displacement field (Image 3) that transforms the unloaded image into the loaded
 123 configuration. The strain field can then be derived from the displacement field (Image 4).

124 2. Materials and Methods

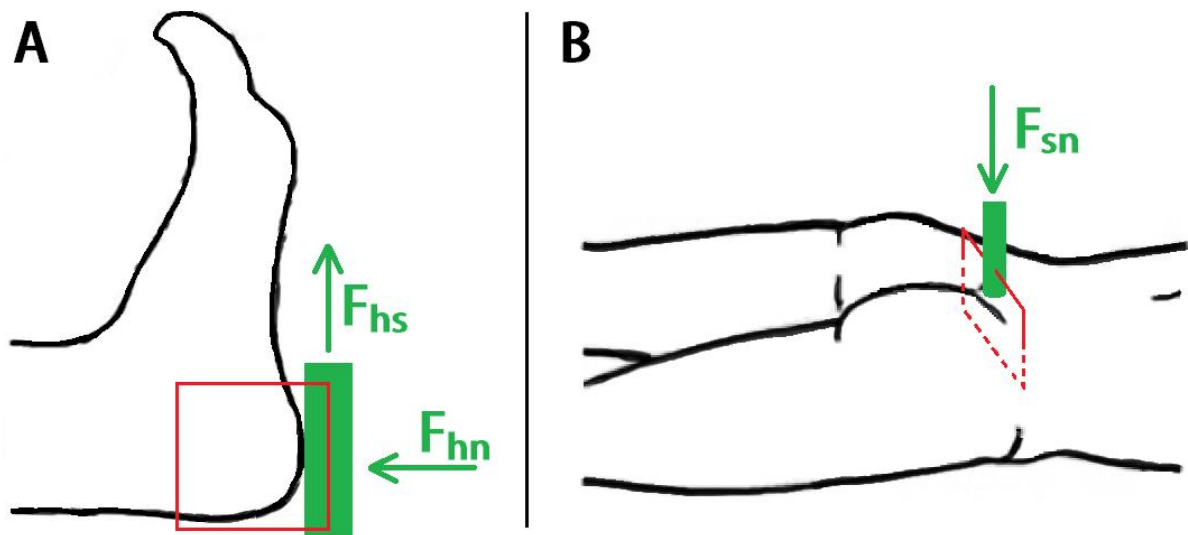
125 2.1. Materials: heel and sacrum MR datasets previously collected on one healthy volunteer

126 The MRI datasets used in this study have been collected in a previous study [17]. For the sake of clarity,
 127 the main details regarding the experimental setup, protocol and participant are summarized in the
 128 following paragraph. For more details, the reader is referred to the associated publication.

129 A healthy volunteer (male, 40 years old) gave his informed consent to participate in the experimental
 130 part of a pilot study approved by an ethical committee (MammoBio MAP-VS pilot study N°ID RCB 2012-
 131 A00340-43, IRMaGe platform, Univ. Grenoble Alpes).

132 For the heel MR image datasets, the volunteer was placed in a supine position with his right foot locked
 133 in a MR compatible device designed to apply both a normal force (15 N) or a combined normal-and-
 134 shearing force (15 N normal + 45 N shearing) on the heel pad by means of an indenting platform. The
 135 setup is illustrated in Figure 2A. A proton density MR sequence was used to collect 3D images
 136 composed of 512 x 428 x 512 voxels with voxel size of 0.3125 mm x 0.375 mm x 0.3125 mm (MRI
 137 system Achieva 3.0T dStream Philips Healthcare). Two acquisitions of the same unloaded configuration
 138 allowed to avoid having the same noise pattern between equivalent images in the subsequent image
 139 registration process in order to test the repeatability of strain calculation.

140 For the sacrum images, the subject was placed in the MR bed in a prone position. An indenter actuated
 141 by gravity applied a normal load (12 N) on the sacrum region. The 3D images were composed by
 142 800x800x240 voxels with a dimension of 0.5 x 0.5 x 0.5 mm Figure 2B. Likewise, two acquisitions were
 143 collected in the unloaded configuration to test the repeatability of strain calculation.



144

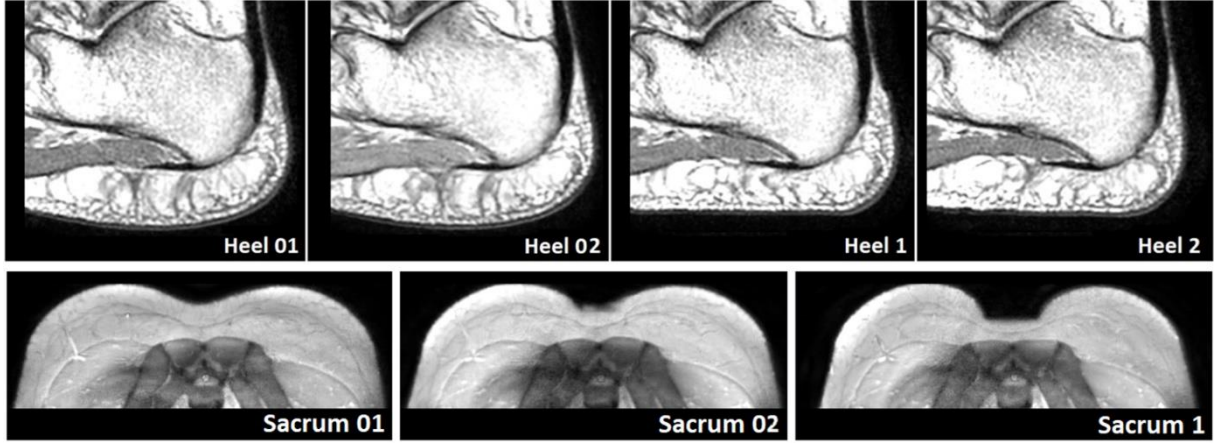
145 Figure 2 : (A) Scheme of the heel configurations during the MR acquisitions. The green rectangle
 146 represents the plate applying the loads. Direction of the loads is represented by the green arrows F_{hn}
 147 (Force heel normal) and F_{hs} (Force heel shear). The red rectangle shows the orientation of the MRI slice
 148 that will be shown in the rest of the paper. (B) Scheme for the sacrum configuration (Analogous to A).
 149 The green block represents the indenter with the respective F_{sn} (Force sacrum normal) applied. The
 150 indenter has the external shape of an ultrasound probe, 10-2 linear probe transducer developed by
 151 (Aixplorer, SuperSonic Imagine, France).

152 Four 3D MR images of the heel and three 3D MR images of the sacrum region were considered in this
 153 contribution and were referred to using a unique name as listed in Table 1.

Name	Description	Load
Heel 01	Unloaded heel – Acquisition 1	0 N
Heel 02	Unloaded heel – Acquisition 2	0 N
Heel 1	Heel with normal load	15 N normal
Heel 2	Heel with normal and shearing load	15 N normal and 45 N shear
Sacrum 01	Unloaded Sacrum – Acquisition 1	0 N
Sacrum 02	Unloaded Sacrum – Acquisition 2	0 N
Sacrum 1	Sacrum with normal load	12 N normal

154 Table 1 : List of MR acquisitions. The first name indicates the body location of the image. The unloaded
 155 configurations are indicated by the initial number 0 (01, 02). The loaded configurations are indicated
 156 by the integer positive numbers (1,2).

157 A 2D snapshot of each MR volume (presented as the red rectangle in Figure 2) is provided in Figure 3.



158

159 Figure 3 : Slices of the heel and the sacrum unloaded and loaded configurations described in Table 1.
 160 The respective region is indicated in Figure 2 by the red rectangle.

161 **2.2. Rigid registration**

162 The four MR volumes of the heel and the three MR volumes of the sacrum were rigidly registered to
 163 align the calcaneus bone and the sacrum bone respectively using the publicly available registration
 164 package Elastix [22].

165 **2.3. Digital Volume Correlation between the loaded and the unloaded MR images**

166 The registration package Elastix [22] was then used to perform DVC. Two images are involved in this
 167 registration process: the reference image $I_0(x)$ (unloaded configuration: Heel/Sacrum 01/02, called
 168 “fixed image” in the Elastix library) and the deformed image, $I_Q(x)$ (loaded configuration: Heel 1 and
 169 2 and Sacrum 1, called “moving image” in the Elastix library), where x represents the position of a
 170 point in the images. The registration between these two images defines a non-rigid deformation field
 171 $u_Q(x)$, which describes how the reference unloaded image transforms into the deformed image.
 172 Applying the deformation field to the reference image creates a transformed-deformed image
 173 $I_0(x + u_Q(x))$ that aims to look identical to the deformed image.

174 The optimal deformation field was estimated by minimizing a cost function by means of an iterative
 175 optimization method (adaptive stochastic gradient descent) embedded in a hierarchical
 176 (multiresolution) scheme. The cost function relates to the similarity between the two images (*i.e.* the
 177 reference image and its transformation) using image features and was based on the Normalized
 178 Correlation Coefficient (NCC).

179 During the optimization step, the value of the cost function was evaluated at non-voxel positions, for
 180 which intensity interpolation with cubic B-Spline was used.

181 **2.4. Computing mechanical strains from the DVC-derived displacement fields**

182 From the displacement fields obtained by the registrations, strain maps were calculated as follows:
 183 The relation between the position X of a material point in the undeformed configuration and its
 184 position x in a deformed configuration Q is described by the spatial displacement vector $u_Q(x)$ which
 185 consists of 3 components u_{Qx}, u_{Qy}, u_{Qz} :

186
$$u_Q(x) = [u_{Qx}, u_{Qy}, u_{Qz}]^T \tag{1}$$

187 From these, the deformation gradient F can be computed:

188 $F = I + \frac{\partial u}{\partial X}$ (2)

189 And the right Cauchy-Green deformation tensor C deduced:

190 $C = F^T F$ (3)

191 The Green Lagrange principal strains:

192 $E_p = eig(\frac{1}{2} (C - I))$ (4)

193 The maximum GL shear strains are defined as:

194 $E_s = \frac{1}{2} * \max(|E_1 - E_2|, |E_1 - E_3|, |E_2 - E_3|)$ (5)

195 **2.5. Uncertainty of the Image registration procedure**

196 To evaluate the uncertainty of the DVC we consider six evaluation Cases A to F. The first three cases
 197 are related to the repetition of the same strain measurement and to the analysis of the differences
 198 between the respective results (reproducibility of the registration). The last three cases focus on the
 199 ability of DVC to estimate a known a priori strain field (accuracy of the registration).

200 **2.5.1. Reproducibility**

201 Reproducibility refers to the closeness of agreement between test results. In this section, we propose
 202 to evaluate the reproducibility of strain calculation through image registration. Two acquisitions of the
 203 unloaded configurations of the heel and sacrum (namely Heel 01 and Heel 02 and sacrum 01 and
 204 sacrum 02 respectively) were registered to the same moving image (Heel 1 and Sacrum 1 respectively).
 205 The corresponding strain maps are computed from the two estimated deformation fields. The
 206 reproducibility is then inspected by analyzing the differences between these two strain maps. Three
 207 cases, summarized in Table 2, are considered: heel under normal load (A), heel under normal+shearing
 208 load (B) and sacrum under normal load (C).

Fixed image	Moving image	Case	Displacement field	Shear strain field
Heel 01	Heel 1	A	DA ₀₁₁	SA ₀₁₁
Heel 02	Heel 1		DA ₀₂₁	SA ₀₂₁
Heel 01	Heel 2	B	DB ₀₁₂	SB ₀₁₂
Heel 02	Heel 2		DB ₀₂₂	SB ₀₂₂
Sacrum 01	Sacrum 1	C	DC ₀₁₁	SC ₀₁₁
Sacrum 02	Sacrum 1		DC ₀₂₁	SC ₀₂₁

209 Table 2 : List of image registrations to evaluate the reproducibility of strain calculation from image
 210 registration. Each line represents an image registration composed by its fixed and moving image. The
 211 tests are grouped in three Cases: A) Heel with normal load, B) Heel with normal+shearing load, C)
 212 Sacrum with normal load. The resulting displacement fields and shearing strain field are respectively
 213 denoted with the letters D and S. The second letter in the field nomenclature reports the respective
 214 case of the registration. The numbers report the name of the fixed and moving images.

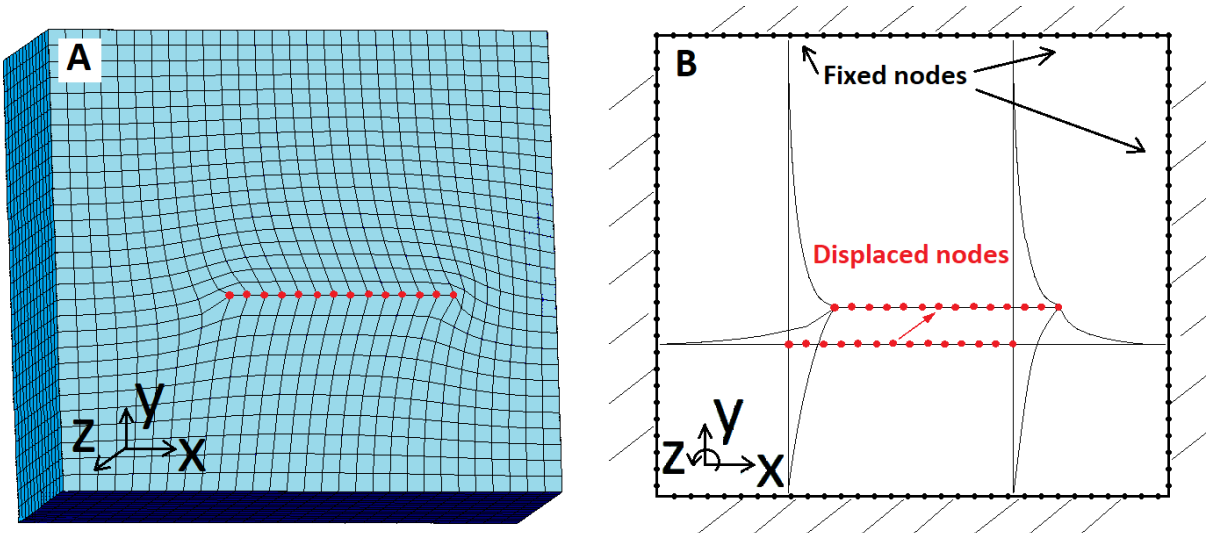
215 **2.5.2. Accuracy**

216 Accuracy reflects how close a data is to a known or accepted value. In this section, we propose to
 217 evaluate the accuracy of our image registration procedure to identify a known *a priori* strain field. We
 218 focus specifically here on the images of the heel. Two different displacement fields are considered:

- 219 1. For the first case, an artificial displacement field D_{FEM} is generated from a Finite Element (FE)
 220 simulation. A rectangular parallelepiped volume with the same size of the 3D MR images is

221 first generated in ANSYS 19.2 APDL (ANSYS, Inc., Canonsburg, PA). This volume is then meshed
 222 with 8-nodes hexahedral elements and a linear elastic material model is implemented. The 3D
 223 mesh is composed of 24389 hexahedral elements. The nodes on the sides of the parallelepiped
 224 are fixed in order to avoid any displacements outside of the defined volume. A set of 196
 225 internal central nodes located on the same XZ plane are then submitted to a prescribed
 226 displacement boundary condition in a normal (Y) and in a tangent (X) direction (Figure 4). The
 227 displacement field computed by ANSYS is then extracted for all the nodes of the parallelepiped
 228 and interpolated to fit the resolution of the MR images. The corresponding displacement field
 229 is applied to the unloaded image (Heel 01) to generate a new artificially loaded image of the
 230 heel, named Heel FEM (Table 3 and Figure 5). It is worth noting that the objective of the FE
 231 method is mainly to produce a known *a priori* displacement field. This displacement field will
 232 be subsequently estimated through the image registration technique. The simulation itself,
 233 and the artificially generated image Heel FEM, do not have any real physical meaning. The
 234 main benefit of using such an FE solver is the possibility to get a ground-truth strain field that
 235 can be compared to values estimated from image registration.

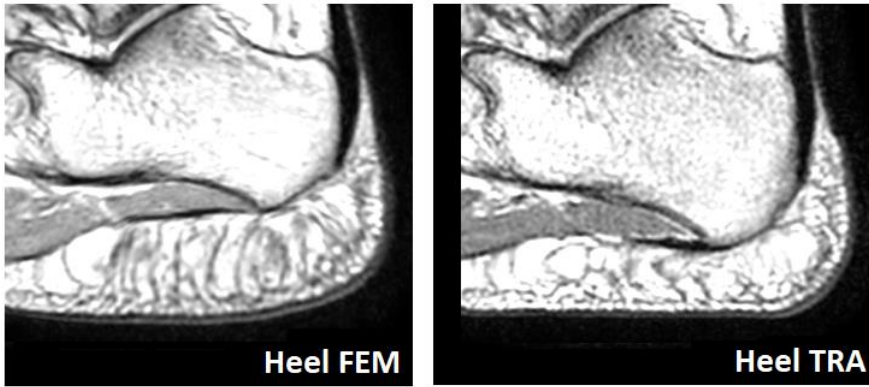
- 236 2. For the second case, the previously computed displacement field DA_{011} is applied to the
 237 unloaded image (Heel 01) to generate a new artificially loaded image of the heel, named Heel
 238 TRA (from the word transformed) (Table 3 and Figure 5).



239
 240 Figure 4 : Generation of an artificial displacement field from a FE simulation generated by Ansys. The
 241 size of the cube matches with the size of the MR images of the heel. A selection of nodes (red dots)
 242 on a plane orthogonal to the y axis was displaced as boundary conditions. (A) Section of the simulated
 243 cube along a plane orthogonal to the z axis. (B) Schematization of the boundary conditions imposed.
 244 The external nodes were fixed, and the selection of red nodes was displaced.

Image	Applied displacement field	Artificial image	Shear strain field
Heel 01	D_{FEM}	Heel FEM	S_{FEM}
Heel 01	DA_{011}	Heel TRA	SA_{011}

245 Table 3 : List of transformations to create the artificial images to test the accuracy of strain calculation
 246 through image registration. The image column lists the images to be transformed. The displacement
 247 field column lists the transformation to be applied to generate the artificially deformed image.



248

249 Figure 5 : Artificial images obtained once the displacement fields D_{FEM} and DA_{011} are applied to the
 250 unloaded image Heel 01.

251 Image registration was then computed between Heel 02 and the two artificially deformed images Heel
 252 FEM and Heel TRA. Note here that having two acquisitions of the same unloaded configuration (Heel
 253 01 and Heel 02) allowed to implement different noise patterns during the registration process in the
 254 fixed and moving image (Cases D and F of Table 4). On the other hand, to show the impact of having
 255 the same noise pattern between the fixed and the moving image the image Heel 01 was also
 256 considered for Case E (table 4).

Fixed	Moving	Case	Displacement field	Shear strain field
Heel 02	Heel FEM	D	DD	SD
Heel 01	Heel FEM	E	DE	SE
Heel 02	Heel TRA	F	DF	SF

257 Table 4 : Following cases A, B and C mentioned in Table 2, cases D, E and F relate to the estimation of
 258 the accuracy of strain calculation through image registration. The shear strain fields SD and SE will be
 259 compared with S_{FEM} . The shear strain fields SF will be compared with SA_{011} .

260 2.5.3. Error quantification

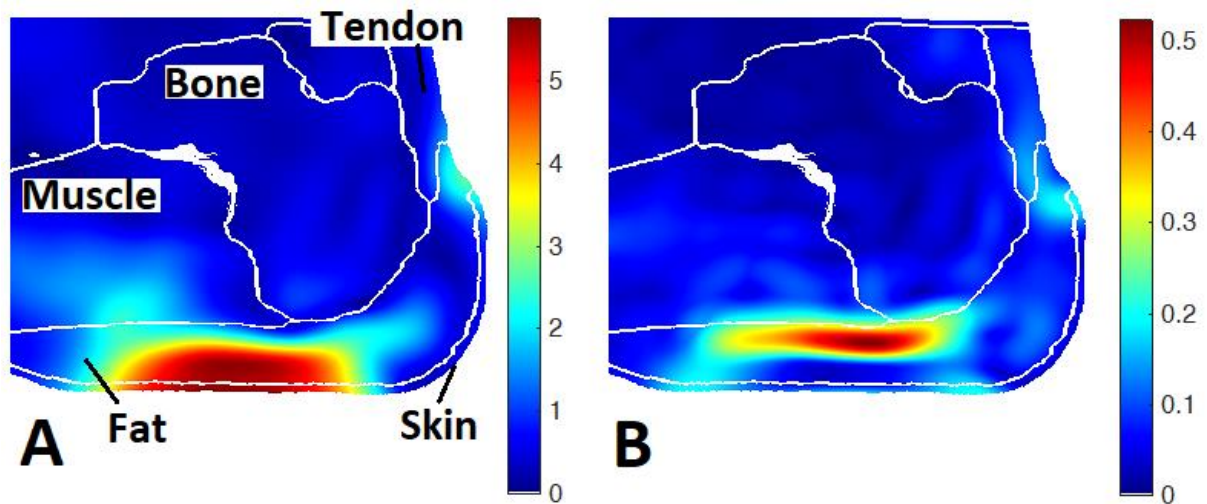
261 The error estimation was performed analyzing the obtained strain fields with a Bland–Altman plot. This
 262 representation is a method of data plotting used in analyzing the agreement between two different
 263 set of data corresponding to the same measurement. The plotted graph shows the error distribution
 264 throughout the whole range of measured strain values.

265

266 3. Results

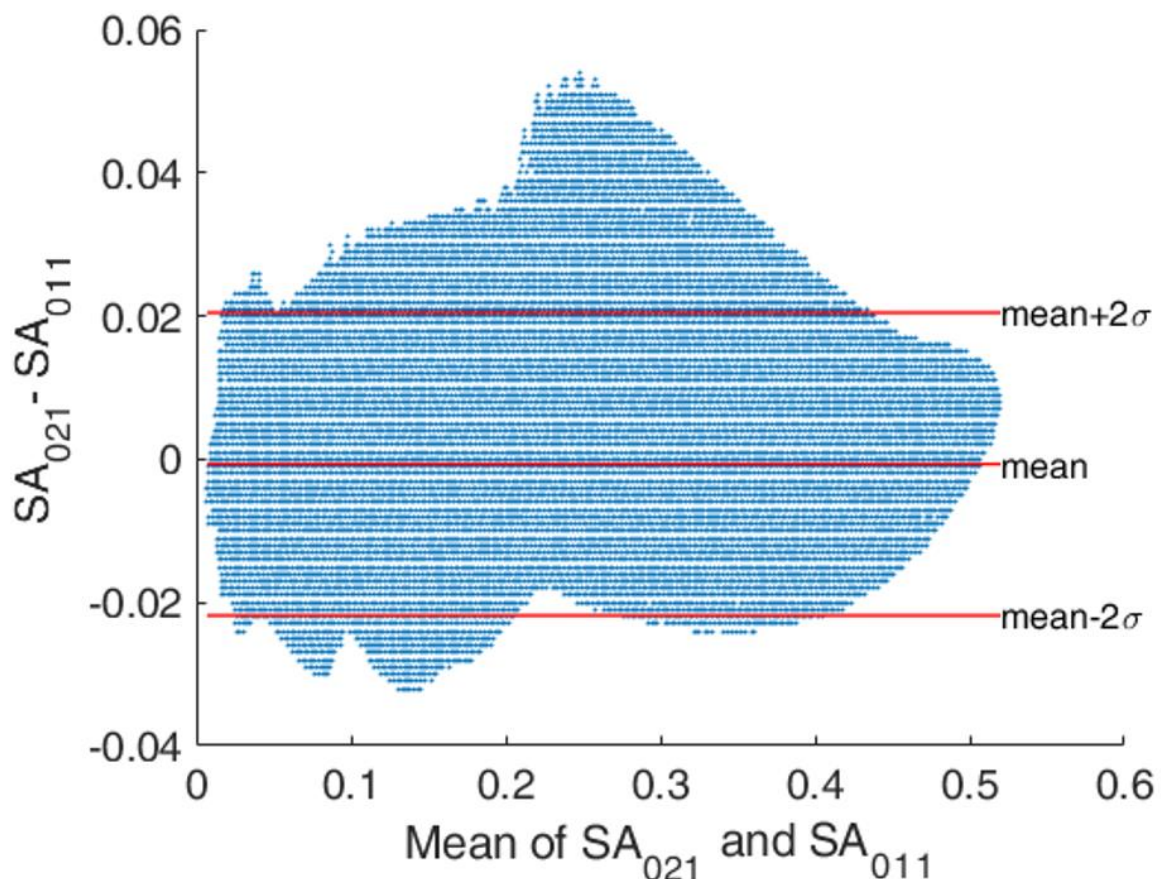
267 3.1. Strain measurements for heel under normal load (case A, Table 2)

268 The distribution of the DVC-derived displacement field in the heel domain under normal load is given
 269 in the sagittal slice containing the highest shear strains (Figure 6A). The highest displacements are
 270 uniform in the area where the plate was in contact with the plantar skin of the heel. Figure 6B shows
 271 the corresponding maximal GL shear strains computed from the displacement field. Shear strains are
 272 concentrated around the lower part of the calcaneus bone propagating towards the plantar fascia and
 273 the flexor digitorum brevis.



274

275 Figure 6 : Case A. Biological tissues are delimited by white lines. A slice from the MR volume is shown
 276 from the sagittal plane corresponding to the location of the highest shear strain. (A) Visual
 277 representation of DA_{011} . Modulus of displacement field [mm] for heel under normal load. (B) Visual
 278 representation of SA_{011} . Max GL shear strain field for heel under normal load (0.5 corresponds to 50%
 279 of deformation).



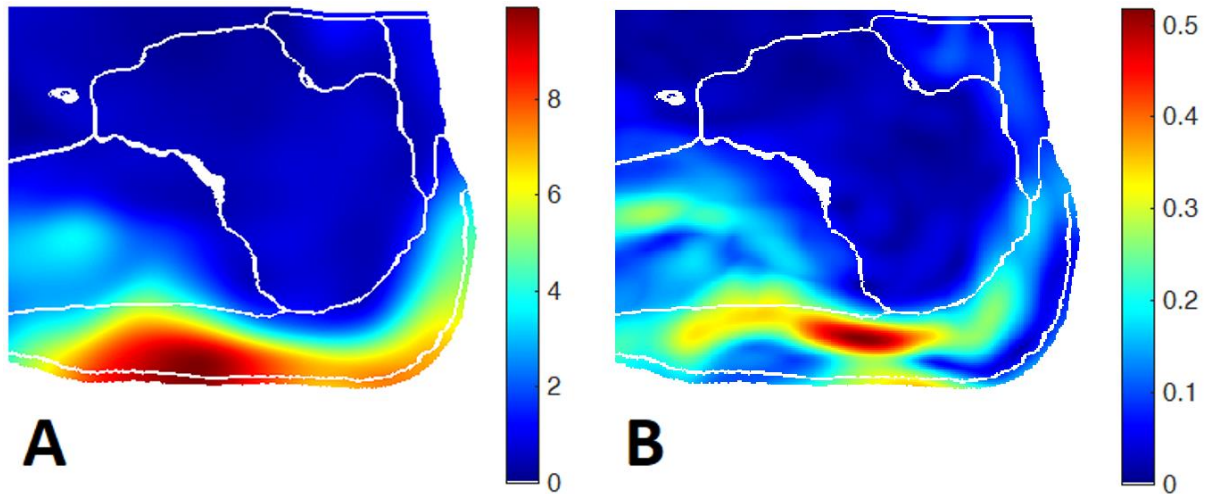
280

281 Figure 7 : Bland-Altman plot referring to the strain estimation computed from Case A: heel under
 282 normal load. The upper and lower red line correspond the 95% confidence interval, meaning that 95%
 283 of the values have an error lower than 0.02 strain. The most relevant part of the plot is the region with
 284 the highest values of the strains 0.4-0.5 as these can represent the threat for tissue damage.

285

286 The agreement between SA_{011} and SA_{021} was described graphically with a Bland-Altman plot (Figure 8)
287 with mean of differences, reported with corresponding 95% confidence interval (CI), and lower and
288 upper limits of agreement, calculated as $\text{mean} \pm 2\sigma$ (where σ represents the standard deviation SD).
289 Differences were assessed using a Wilcoxon-Signed-Rank Test (paired data) at the default 5 %
290 significance level.

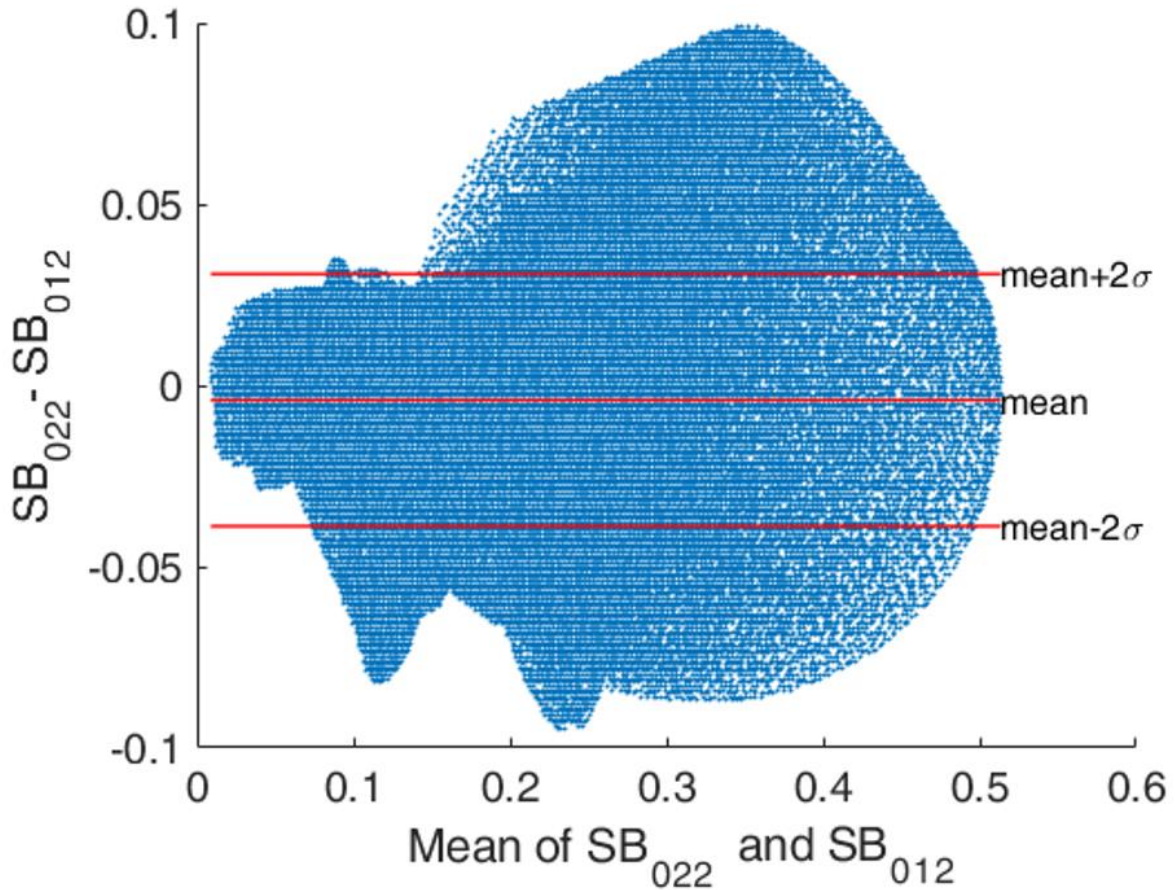
291 **3.2. Strain measurements for heel under normal+shearing load (case B, Table 2)**



292

293 Figure 9 : (A) Modulus (in mm) of displacement field for heel under shearing load DB_{012} . (B) Max GL
294 shear strain field for heel under shearing load SB_{012} .

295 The application of the shearing load had a relevant impact on the soft tissue displacements. The plate
296 moved the posterior and the plantar regions of the heel skin towards the forefoot. This caused the
297 shear strains to propagate on a wider region of the fat pad and the muscle (Figure 9). A concentration
298 of high levels of strains is found in the fat pad under the flexor digitorum brevis.



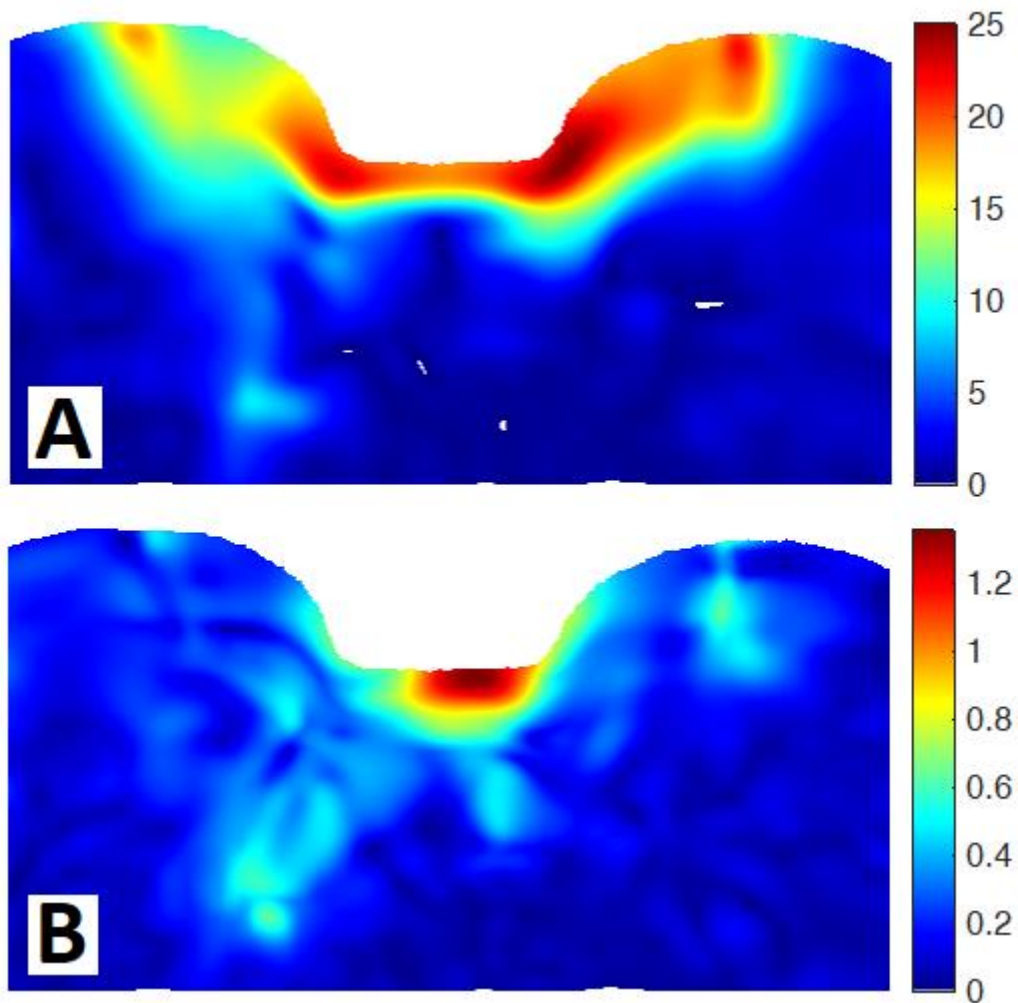
299

300 Figure 10 : Bland-Altman plot referring to the strain estimation computed from Case B: heel under
 301 normal+shearing load. Error magnitude is around twice higher than the configuration with normal load
 302 only (Figure 7).

303 Figure 10 shows the correlation between the strain measurements of the heel under normal+shearing
 304 loads (Case B of Table 2). Errors of 0.1 are observed across most of the strain intensities even for the
 305 highest strains (around 0.5). These errors tend to narrow down for the peak values. The SD shows that
 306 95% of voxels have a strain error lower than 0.04. In general, this shearing configuration (Case B) shows
 307 errors with a double intensity and twice the propagation with respect to the normal load configuration
 308 (Case A).

309 3.3. Strain measurements for sacrum under normal load (case C, Table 2)

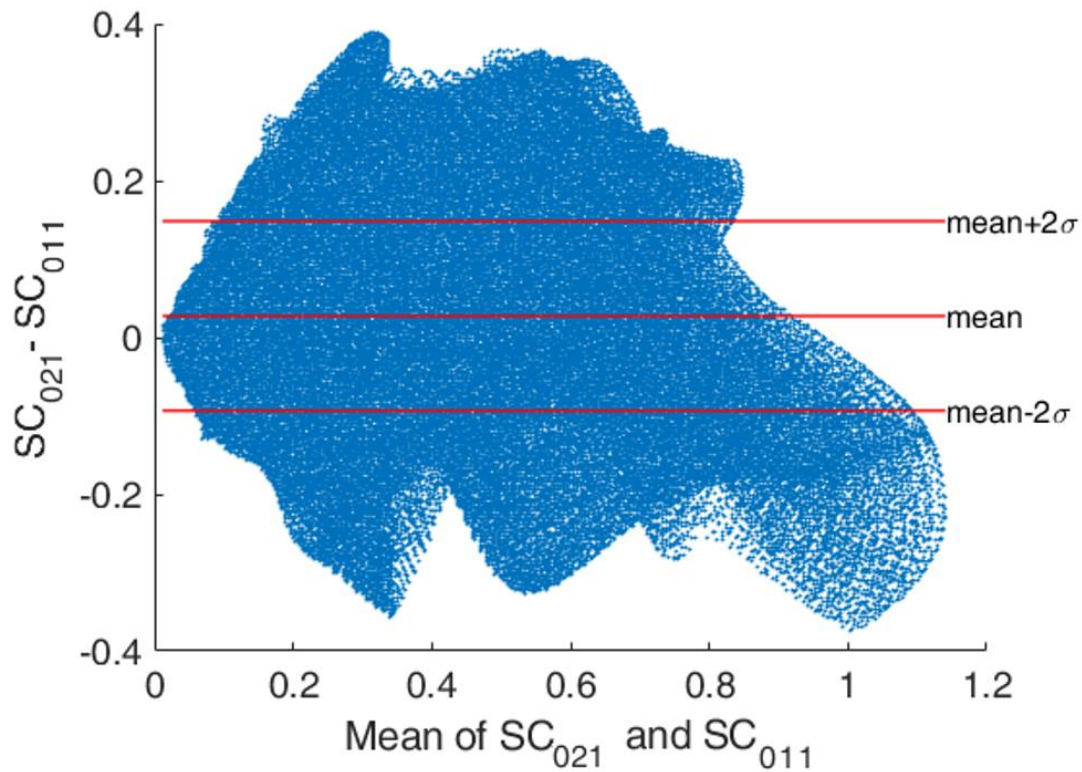
310 For the sacrum loading configuration (Figure 11), the highest levels of displacements are found around
 311 the edges of the indenter. Shear strains are concentrated on the soft tissues around the contact area
 312 between the indenter and the skin. Adipose tissue and skin are subject to the highest levels of strains.



313

314 Figure 11 : (A) Modulus (in mm) of displacement field for sacrum under normal load DC_{011} . (B) Max GL
 315 shear strain field for sacrum under normal load SC_{011} .

316 Figure 12 presents the Bland-Altman plot between the shear strain measurements produced by an
 317 indenter on the sacrum region (Case C of Table 2). In this case, the errors are considerably higher than
 318 what was observed for the heel application. Errors of 0.3 are spread throughout the image and the SD
 319 describes an error distribution where 95% of the voxels have an error that is lower than 0.15.

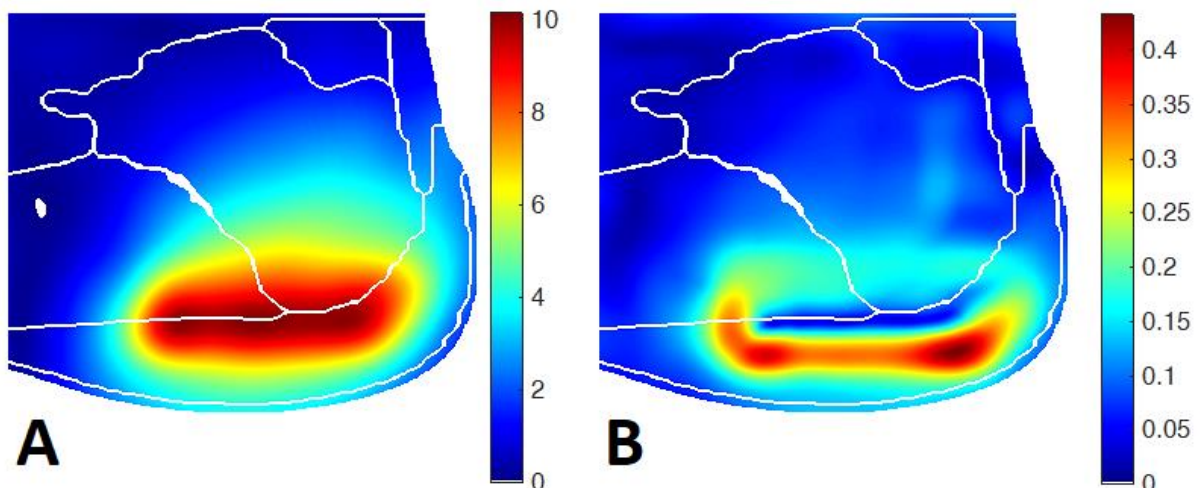


320

321 Figure 12 : Bland-Altman plot referring to the strain estimation computed from Case C: sacrum under normal load.
 322 Errors are considerably higher than for previous configurations of the heel.

323 **3.4. Estimation of strain field generated by the FE model (case D, Table 4)**

324 Figure 13 shows the results of image registration in the estimation of the artificial displacement field
 325 generated by Ansys (Figure 4). Magnitudes of displacements were selected in order to generate strains
 326 comparable with Cases A and B.

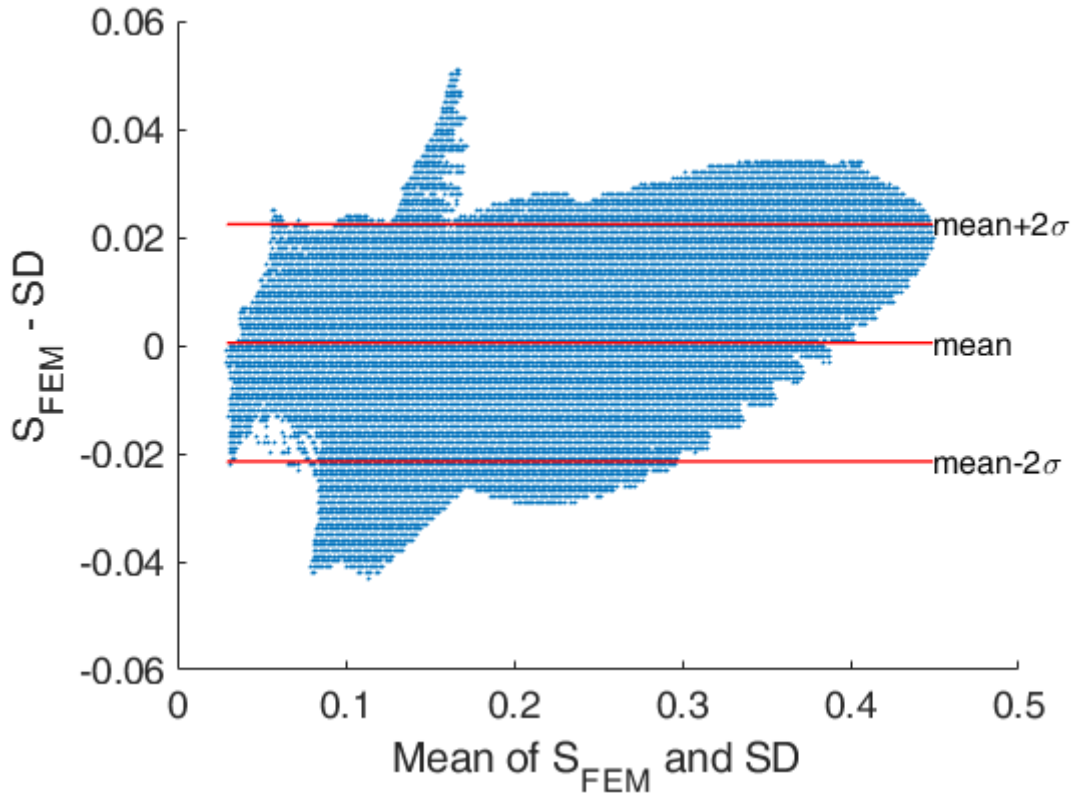


327

328 Figure 13 : (A) Estimation of the displacement field (mm) generated by Ansys DD. (B) Estimation of GL
 329 max shear strain generated by Ansys SD.

330 Figure 13 presents the correlation between the strain field calculated by Ansys and the corresponding
 331 measurements obtained by image registration (Case D of Table 4). The error distribution is comparable

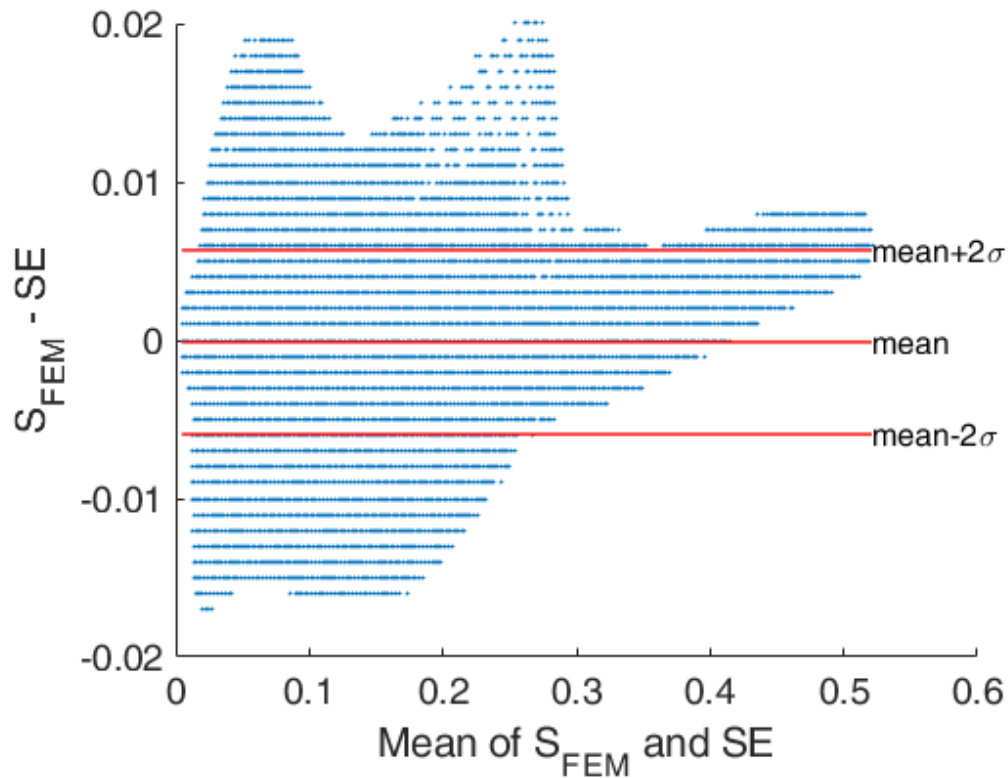
332 to Case A. For the regions with the highest levels of strains, the measurements slightly underestimate
 333 the strains since the points distribution shows an inclination that is higher than the red line. This artifact
 334 could be a result of the transformation step described in Table 3. In this process, some details of the
 335 original displacement field could have been lost in the image reconstruction after the application of
 336 the displacement to the respective voxels.



337
 338 Figure 14 : Bland-Altman plot referring to the strain estimation computed from Case D: Displacement
 339 field generated by Ansys. The intensity of errors is around 0.02, which is comparable with case A (Figure
 340 7).

341 **3.5. Deformation field from Ansys – Same noise pattern (case E, Table 4)**

342 This case is running the registration between two images with the same noise pattern, undeformed
 343 (Heel 01), and artificially deformed (Heel FEM). Using the same image helps considerably the
 344 algorithms of the image registration process since the noise pattern present in the unloaded image
 345 matches the one of the unloaded image. This allows to easily identify the respective deformation
 346 matching the voxels with their equivalent copy in the respective deformed image. Results in terms of
 347 error distribution are as expected very precise showing a relevant strain field estimation (Figure 15).
 348 This reflects the described facilitations in terms of using an image and its deformed version in the
 349 registration process.

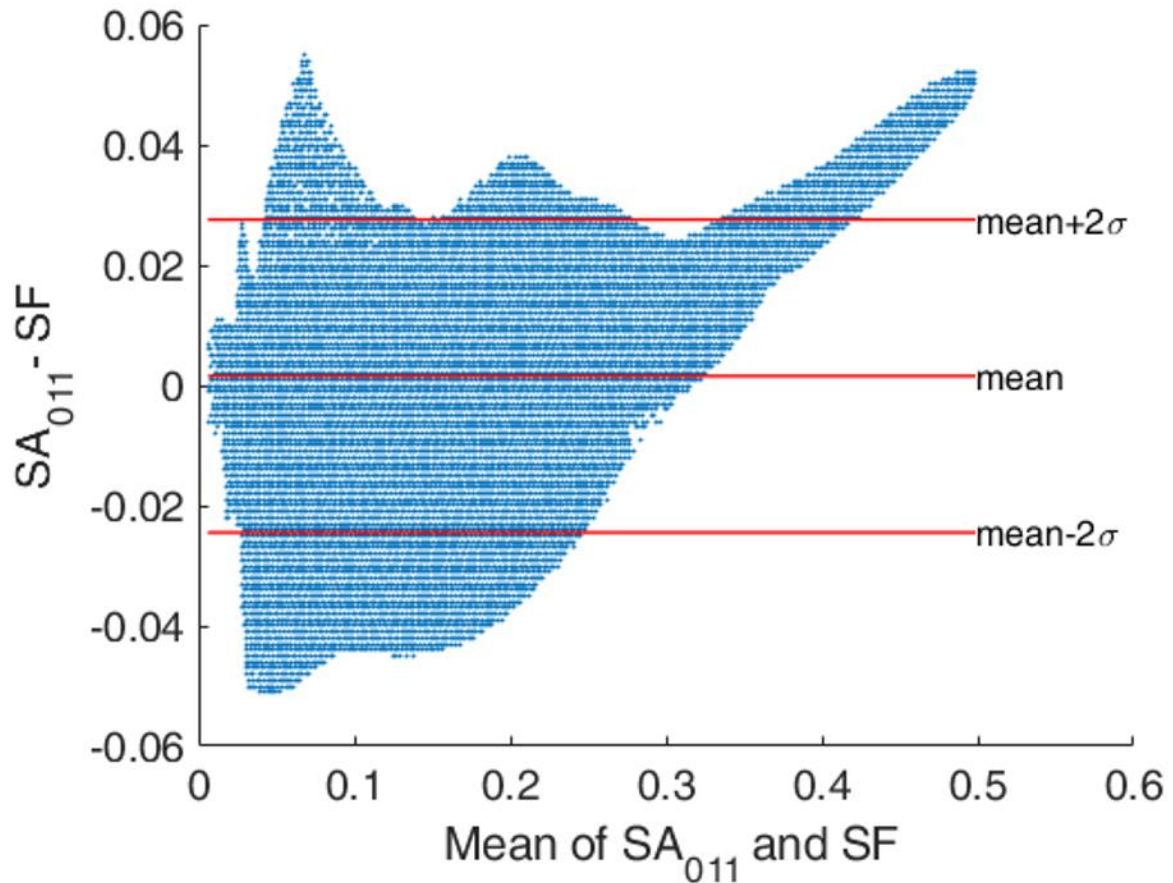


350

351 Figure 15 : Bland-Altman plot referring to the strain estimation computed from Case E: Displacement
 352 field generated by Ansys. Errors are lower than the other considered cases. This is due to the same
 353 noise pattern between the fixed and moving image in the registration procedure.

354 **3.6. Deformation field from Elastix (case F, Table 4)**

355 Case F is analogous to Case D with the main difference that the considered displacement field is not
 356 generated by Ansys but is taken from the image registration computed in Case A. The error distribution
 357 in terms of maximal error and SD is comparable to Case A (Figure 16). For the regions with the highest
 358 levels of strains, as detected also in case D, the measurements slightly underestimate the strains. In
 359 this case, the deformed image is also the result of an image transformation reported in Table 3.



360

361 Figure 16 : Bland-Altman plot referring to the strain estimation computed from Case F: Displacement
 362 field generated by Elastix in Case A. The intensity of errors is around 0.02 comparable with Case A and
 363 D (resp. Figure 7 and Figure 14). This shows that, in the analyzed cases, similar images (Heel 01, 02, 1)
 364 generate errors of comparable magnitude (0.02).

365 4. Discussion

366 In this study, a method to estimate 3D internal tissue strains in the heel and sacrum regions based on
 367 DVC-derived displacement fields was developed in the context of pressure ulcers etiology. The
 368 methodology to implement DVC between two MR exams of human soft tissues (one at rest and the
 369 other one deformed) and to estimate the internal strains from the DVC 3D displacement field was first
 370 described. The implemented methodology requires a MR compatible device to apply loading on the
 371 skin surface during the acquisition of MR images. The obtained acquisitions were then used as input
 372 for 3D image registration. Images were first aligned based on the fixed body part (like bones) and then
 373 the non-rigid transformation was calculated. This transformation consists of a displacement field
 374 mapping every voxel between its initial position in the unloaded image and its final position in the
 375 loaded image. The GL shear strains are then computed from this displacement field. This methodology
 376 was implemented to analyze strain propagation in body regions that are critical in terms of pressure
 377 ulcer development: heel and sacrum.

378 For the results related to the heel pad, the calculated strain maps show as expected shear and
 379 compressive strain concentrations around the bony prominences of the calcaneus. This is coherent
 380 with the study of Luboz et al. which highlighted that strains generated around the calcaneus head
 381 strongly depended on the shape of this calcaneus bone [23]. Strains values in the deep tissues of the
 382 human heel were considerably higher than those in superficial tissue layers (Figure 6B). This is

383 consistent with previous findings listing the strain concentration in deep tissues as a key aspect in the
384 etiology of ulceration [24]. The strains were concentrated in the fat pad region and propagating
385 towards the interface with the muscular region. Oomens et al. identified skeletal muscle and fat as the
386 two main biological tissues where pressure ulcers could develop [25]. The application of a shearing
387 load pushing the first layer of skin towards the forefoot generated significantly higher shearing loads
388 in the anterior region of the fat pad compared with the configuration with only normal plantar
389 pressure. Shear loadings can therefore impact significantly wider regions with higher levels of shear
390 strains compared with normal loads of comparable intensity. This confirms what Ceelen et al. stated,
391 namely (1) that shearing loads are more dangerous to treat than normal loadings, in terms of shear
392 strain concentrations, and (2) that they must be taken into consideration for an effective pressure ulcer
393 prevention [26].

394 For the results related to the sacrum, the calculated displacement and strain maps have values that
395 are significantly higher than the results from the heel. The application of a load by means of an
396 indentation device with a small contact area is probably more likely to generate higher shear strains
397 right on the contact surface between the skin and the indenter [26].

398 The second objective of this article was to evaluate in a general way the reproducibility and the
399 accuracy of strain calculation through image registration. Respectively, two main methodologies were
400 presented: one related to the repetition of the same strain measurement from an equivalent set of
401 images, and the other one to the calculation of a known *a priori* displacement field.

402 Concerning reproducibility as how much two equivalent measurement match, Figure 7Figure 10Figure
403 12 are considered. Comparing the strain error distribution between image registrations of the heel
404 related to Case A and Case B, we found that errors are twice higher and more distributed in the case
405 where the shearing load is applied. This suggests that strain measurement from image registration is
406 affected by the type of deformation applied on the soft tissues. A possible explanation for this effect
407 can be related to the fact that a normal load displaces the skin in a normal direction generating a clear
408 displacement of the edge between the portion of image representing the biological tissues and the
409 dark background (see Figure 3 Heel 01 and Heel 1). On the other hand, a shear load displaces the skin
410 only in a tangent direction to the surface of the skin without generating any clear movement of the
411 edge between the skin and the background (see Figure 3 Heel 1 and Heel 2).

412 The image registration related to the sacrum has a much wider strain error distribution and values
413 compared to the examples of the heel. This implies that strain measurement from image registration
414 strongly depends on the image characteristics. To explain the reasons behind this we can try to analyze
415 how image registration works. The first steps in the algorithms of image registration are feature
416 detection and feature matching [27]. Salient and distinctive objects as edges are considered as
417 features. The accuracy of image registration therefore directly depends on the quality of the acquired
418 images to define clearly these edges [28]. The main parameters that characterize the quality of digital
419 images are related to resolution and noise [29]. Noise is generated by the statistical fluctuation of the
420 value from voxel to voxel. A common measurement of noise is the standard deviation, a measure of
421 how spread out the values of the pixels are. The lower the standard deviation, the higher the accuracy
422 of the average voxel value [30]. Spatial resolution is the ability of the imaging system to detect small
423 objects that are close to each other [31]. The size of the voxels defines the maximum spatial resolution.
424 However, image resolution is also influenced by other parameters such as blur factors. The most
425 common blur factor is motion blur: when motion occurs during acquisition, the boundaries of patient
426 structures will move from their initial position, making the boundaries blurred in the image. The
427 motion can in general be reduced by fixing the body part with heavy MR-compatible pillows or casts
428 [16]. These solutions, however, are ineffective when motions are generated by physiological
429 movements such as breathing, peristalsis or heart beats. The line spread function (LSF) can be used to
430 evaluate and quantify spatial resolution [32][33]. From this parameter, it was calculated that in the

431 more crucial region of the images, the MR image of the heel had a quality parameter related to the
432 spatial resolution that was 4.5 time higher than the one calculated for the sacrum images. It is possible
433 therefore that this aspect played a crucial role in the strain estimation through image registration, thus
434 decreasing significantly its reproducibility.

435 Concerning accuracy as how close a measurement is to a known or accepted value, Cases D and F were
436 considered. These cases report errors of shearing strains around 0.02. This value can be compared to
437 the level of strains that is considered to be sufficient to generate significant tissue damage. According
438 to Ceelen et al., this value is around 0.65 for the shearing strain [5].

439 An interesting aspect is related to Case E, which uses the same image Heel 01 and its transformed
440 version (Heel TRA) for the estimation of the displacement field. In this case, the strain errors are much
441 less distributed (with a 95% confidence value below 0.007 error). This is due to the fact that any
442 variability due to noise, or other artifacts, present in both images will have an impact on the strain
443 estimation. This implies that for images with appropriate quality levels, this methodology can reach
444 high accuracy.

445 The diversity of results obtained between the heel and sacrum applications implies that crucial further
446 research is therefore required in finding the relation between specific image quality parameters and
447 the respective error distribution in the strain calculation. This would permit in fact to select the image
448 acquisition protocols in order to obtain the type of images to minimize errors in the registration
449 process.

450 An advantage of the proposed methodology to calculate strains is that no additional tool to perform
451 the error estimation is required. Considering Case E, the error estimation can be performed just with
452 an additional image transformation (Table 3) and the respective image registration.

453 It is clear that the accuracy of the results is strongly related to the image registration process and to
454 the selected parameters to perform it. By tuning the respective parameters of the registration process,
455 it is possible to identify smaller deformations or to select the amount of volume compression and
456 expansion. An optimization for the selection of the ideal parameters of the registration for the related
457 application will be considered in the future steps to improve the accuracy of this methodology.

458 It must be considered that this work was based on specific mechanical configurations of a single subject
459 meaning that results obtained are to be considered specific to this application. Fat and muscle
460 biomechanical properties can change significantly as a consequence of diseases (for example,
461 diabetes) and chronic immobilizations [34][35]. This inter-subject variability may introduce significant
462 variations in the strain calculations making imperative to analyze each subject specifically.

463

464 **5. Conclusion**

465 The results obtained from the practical application on the heel and sacrum, in terms of location and
466 magnitude of strains, are in line with the literature. This technique of calculating strains offers broad
467 new possibilities to analyze the impact of external loads on the internal state of the soft tissues. The
468 standard technique of FE is a very complex and time-consuming task involving segmentations, meshing
469 and selections of proper constitutive laws. The possibility of strain calculation through image
470 registration can provide results in terms of strain propagation in a significantly faster framework and
471 offer the possibility for comparison and validation with results obtained from FE simulations. The
472 present study proposed to quantify subdermal tissue strain distributions on the heel and sacrum from
473 image registrations based on MR-acquisitions. This data is crucial for understanding the etiology of
474 pressure ulcers that occur in the deep tissues of the heel pad.

475 The pilot study described here indicates that the crucial steps for computing strains from image
476 registration are feasible to be implemented in a wider study. Further research will include analysis on

477 more subjects and with different loading configurations, together with the adaptation of this
478 methodology to different parts of the body to gain insight into the relative mechanical soft tissue
479 properties.

480

481 **Acknowledgments**

482 This research has received funding from the European Union's Horizon 2020 research and innovation
483 programme under the Marie Skłodowska-Curie Grant Agreement No. 811965; project STINTS (Skin
484 Tissue Integrity under Shear). IRMaGe MRI facility was partly funded by the French program
485 "Investissement d'Avenir" run by the "Agence Nationale pour la Recherche"; grant "Infrastructure
486 d'avenir en Biologie Sante" - ANR-11-INSB-0006.

487

488 **Conflict of interest**

489 None

490 **Ethical approval**

491 A volunteer (male, 40 years old) agreed to participate in an experiment part of a pilot study
492 approved by an ethical committee (MammoBio MAP-VS pilot study). He gave his informed
493 consent to the experimental procedure as required by the Helsinki declaration (1964) and
494 the local Ethics Committee.

495

496 **References**

- 497 [1] Barczak CA, Barnett RI, Childs EJ, Bosley LM. Fourth national pressure ulcer prevalence survey.
498 *Adv Wound Care* 1997;10:18–26.
- 499 [2] Dugaret E, Videau MN, Faure I, Gabinski C, Bourdel-Marchasson I, Salles N. Prevalence and
500 incidence rates of pressure ulcers in an Emergency Department. *Int Wound J* 2014;11:386–91.
501 <https://doi.org/10.1111/J.1742-481X.2012.01103.X>.
- 502 [3] Vanderwee K, Clark M, Dealey C, Gunningberg L, Defloor T. Pressure ulcer prevalence in
503 Europe: A pilot study. *J Eval Clin Pract* 2007. [https://doi.org/10.1111/j.1365-](https://doi.org/10.1111/j.1365-2753.2006.00684.x)
504 [2753.2006.00684.x](https://doi.org/10.1111/j.1365-2753.2006.00684.x).
- 505 [4] Thompson D. A critical review of the literature on pressure ulcer aetiology.
506 [Http://DxDoiOrg/1012968/Jowc200514226735](http://DxDoiOrg/1012968/Jowc200514226735) 2013;14:87–90.
507 <https://doi.org/10.12968/JOWC.2005.14.2.26735>.
- 508 [5] Ceelen KK, Stekelenburg A, Loerakker S, Strijkers GJ, Bader DL, Nicolay K, et al. Compression-
509 induced damage and internal tissue strains are related. *J Biomech* 2008;41:3399–404.
510 <https://doi.org/10.1016/J.JBIOMECH.2008.09.016>.
- 511 [6] Gefen A. The biomechanics of heel ulcers. *J Tissue Viability* 2010.
512 <https://doi.org/10.1016/j.jtv.2010.06.003>.
- 513 [7] Fougeron N, Connesson N, Chagnon G, Alonso T, Pasquinet L, Bahuon M, et al. New pressure
514 ulcers dressings to alleviate human soft tissues: A finite element study. *J Tissue Viability*

- 515 2022;31:506–13. <https://doi.org/10.1016/J.JTV.2022.05.007>.
- 516 [8] Keenan BE, Evans SL, Oomens CWJ. A review of foot finite element modelling for pressure
517 ulcer prevention in bedrest: Current perspectives and future recommendations. *J Tissue*
518 *Viability* 2021. <https://doi.org/10.1016/J.JTV.2021.06.004>.
- 519 [9] Savonnet L, Wang X, Duprey S. Finite element models of the thigh-buttock complex for
520 assessing static sitting discomfort and pressure sore risk: a literature review. <https://doi.org/10.1080/10255842.2018.1466117>
521 *OrgSid2nomade-1GrenetFr/101080/1025584220181466117* 2018;21:379–88.
522 <https://doi.org/10.1080/10255842.2018.1466117>.
- 523 [10] Rma A-D, Affiliations PG. A Comprehensive Literature Review of the Pelvis and the Lower
524 Extremity FE Human Models under Quasi-static Conditions 2012.
525 <https://doi.org/10.3233/WOR-2012-1039-4218>.
- 526 [11] Perrier A, Luboz V, Bucki M, Cannard F, Vuillerme N, Payan Y. Biomechanical Modeling of the
527 Foot. *Biomech. Living Organs Hyperelastic Const. Laws Finite Elem. Model.*, 2017.
528 <https://doi.org/10.1016/B978-0-12-804009-6.00025-0>.
- 529 [12] Macron A, Pillet H, Doridam J, Rivals I, Sadeghinia MJ, Verney A, et al. Is a simplified Finite
530 Element model of the gluteus region able to capture the mechanical response of the internal
531 soft tissues under compression? *Clin Biomech* 2020;71:92–100.
532 <https://doi.org/10.1016/J.CLINBIOMECH.2019.10.005>.
- 533 [13] Linder-Ganz E, Shabshin N, Itzchak Y, Gefen A. Assessment of mechanical conditions in sub-
534 dermal tissues during sitting: A combined experimental-MRI and finite element approach. *J*
535 *Biomech* 2007. <https://doi.org/10.1016/j.jbiomech.2006.06.020>.
- 536 [14] Stekelenburg A, Strijkers GJ, Parusel H, Bader DL, Nicolay K, Oomens CW. Role of ischemia and
537 deformation in the onset of compression-induced deep tissue injury: MRI-based studies in a
538 rat model. *J Appl Physiol* 2007. <https://doi.org/10.1152/jappphysiol.01115.2006>.
- 539 [15] Chatzistergos PE, Naemi R, Chockalingam N. An MRI compatible loading device for the
540 reconstruction of clinically relevant plantar pressure distributions and loading scenarios of the
541 forefoot. *Med Eng Phys* 2014. <https://doi.org/10.1016/j.medengphy.2014.06.006>.
- 542 [16] Petre M, Erdemir A, Cavanagh PR. An MRI-compatible foot-loading device for assessment of
543 internal tissue deformation. *J Biomech* 2008. <https://doi.org/10.1016/j.jbiomech.2007.09.018>.
- 544 [17] Trebbi A, Perrier A, Bailet M, Payan Y. MR-compatible loading device for assessment of heel
545 pad internal tissue displacements under shearing load. *Med Eng Phys* 2021;98:125–32.
546 <https://doi.org/10.1016/J.MEDENGPY.2021.11.006>.
- 547 [18] Tavana S, Clark JN, Prior J, Baxan N, Masouros SD, Newell N, et al. Quantifying deformations
548 and strains in human intervertebral discs using Digital Volume Correlation combined with MRI
549 (DVC-MRI). *J Biomech* 2020;102:109604. <https://doi.org/10.1016/J.JBIOMECH.2020.109604>.
- 550 [19] Yoder JH, Peloquin JM, Song G, Tustison NJ, Moon SM, Wright AC, et al. Internal three-
551 dimensional strains in human intervertebral discs under axial compression quantified
552 noninvasively by magnetic resonance imaging and image registration. *J Biomech Eng*
553 2014;136. <https://doi.org/10.1115/1.4028250/371076>.
- 554 [20] Schulz G, Crooijmans HJA, Germann M, Scheffler K, Müller-Gerbl M, Müller B. Three-
555 dimensional strain fields in human brain resulting from formalin fixation. *J Neurosci Methods*
556 2011;202:17–27. <https://doi.org/10.1016/J.JNEUMETH.2011.08.031>.
- 557 [21] Yaman A, Ozturk C, Huijing PA, Yucesoy CA. Magnetic resonance imaging assessment of

- 558 mechanical interactions between human lower leg muscles in vivo. *J Biomech Eng* 2013;135.
559 <https://doi.org/10.1115/1.4024573/370990>.
- 560 [22] Klein S, Staring M, Murphy K, Viergever MA, Pluim JPW. Elastix: A toolbox for intensity-based
561 medical image registration. *IEEE Trans Med Imaging* 2010.
562 <https://doi.org/10.1109/TMI.2009.2035616>.
- 563 [23] Luboz V, Perrier A, Bucki M, Diot B, Cannard F, Vuillerme N, et al. Influence of the Calcaneus
564 Shape on the Risk of Posterior Heel Ulcer Using 3D Patient-Specific Biomechanical Modeling.
565 *Ann Biomed Eng* 2015. <https://doi.org/10.1007/s10439-014-1182-6>.
- 566 [24] Stekelenburg A, Gawlitta D, Bader DL, Oomens CW. Deep Tissue Injury: How Deep is Our
567 Understanding? *Arch Phys Med Rehabil* 2008;89:1410–3.
568 <https://doi.org/10.1016/J.APMR.2008.01.012>.
- 569 [25] Oomens CWJ, Bader DL, Loerakker S, Baaijens F. Pressure Induced Deep Tissue Injury
570 Explained. *Ann Biomed Eng* 2015. <https://doi.org/10.1007/s10439-014-1202-6>.
- 571 [26] Ceelen KK, Stekelenburg A, Loerakker S, Strijkers GJ, Bader DL, Nicolay K, et al. Compression-
572 induced damage and internal tissue strains are related. *J Biomech* 2008;41:3399–404.
573 <https://doi.org/10.1016/J.JBIOMECH.2008.09.016>.
- 574 [27] Oliveira FPM, Tavares JMRS. Medical image registration: a review. <https://doi.org/10.1080/102558422012670855>
575 *OrgSid2nomade-1GrenetFr/101080/102558422012670855* 2013;17:73–93.
576 <https://doi.org/10.1080/10255842.2012.670855>.
- 577 [28] Nederveen AJ, Avril S, Speelman L. MRI strain imaging of the carotid artery: Present
578 limitations and future challenges. *J Biomech* 2014;47:824–33.
579 <https://doi.org/10.1016/J.JBIOMECH.2014.01.014>.
- 580 [29] Goldman LW. Principles of CT: Radiation Dose and Image Quality. *J Nucl Med Technol*
581 2007;35:213–25. <https://doi.org/10.2967/JNMT.106.037846>.
- 582 [30] Alsleem H, Davidson R. Quality parameters and assessment methods of digital radiography
583 images. *Radiographer* 2012;59:46–55. <https://doi.org/10.1002/J.2051-3909.2012.TB00174.X>.
- 584 [31] Williams MB, Krupinski EA, Strauss KJ, Breeden WK, Rzeszotarski MS, Applegate K, et al. Digital
585 Radiography Image Quality: Image Acquisition. *J Am Coll Radiol* 2007;4:371–88.
586 <https://doi.org/10.1016/J.JACR.2007.02.002>.
- 587 [32] Samei E, Ranger NT, Dobbins JT, Chen Y. Intercomparison of methods for image quality
588 characterization. I. Modulation transfer functiona). *Med Phys* 2006;33:1454–65.
589 <https://doi.org/10.1118/1.2188816>.
- 590 [33] Nugent PW, Shaw JA, Kehoe MR, Smith CW, Moon TS, Swanson RC. Measuring the
591 modulation transfer function of an imaging spectrometer with rooflines of opportunity.
592 <https://doi.org/10.1117/1.3497051>
593 *OrgSid2nomade-1GrenetFr/101117/13497051* 2010;49:103201.
- 594 [34] Fontanella CG, Nalesso F, Carniel EL, Natali AN. Biomechanical behavior of plantar fat pad in
595 healthy and degenerative foot conditions. *Med Biol Eng Comput* 2016.
596 <https://doi.org/10.1007/s11517-015-1356-x>.
- 597 [35] Talmadge RJ, Roy RR, Caiozzo VJ, Reggie Edgerton V. Mechanical properties of rat soleus after
598 long-term spinal cord transection. *J Appl Physiol* 2002.
599 <https://doi.org/10.1152/jappphysiol.00053.2002>.

600